Enhanced Photocatalytic Activity of Surface-Modified TiO2 with Bimetallic AuPd Nanoalloys for Hydrogen Generation

Ana Andrea Méndez-Medrano, Daniel Bahena-Uribe, Diana Dragoe, Carine Clavaguéra, Christophe Colbeau-Justin, Juan Pedro Palomares Báez, José Luis Rodríguez-López, Hynd Remita

Enhanced Photocatalytic Activity of Surface-Modified TiO_2 with Bimetallic AuPd Nanoalloys for Hydrogen Generation

Ana Andrea Méndez-Medrano, Daniel Bahena-Uribe, Diana Dragoe, Carine Clavaguéra, Christophe Colbeau-Justine, Juan Pedro Palomares Báez, José Luis Rodríguez-López, [*] *Hynd Remita* [*]

A. A. M. M., Dr. C. C., Prof. C. C. J, Prof. H. R.
Institut de Chimie Physique, UMR 8000 CNRS
Université Paris-Saclay, 91405 Orsay, France.
E-mail: hynd.remita@universite-paris-saclay.fr

A. A. M. M., Prof. J. L. R. L.
Advanced Materials Department
Instituto Potosino de Investigación Científica y Tecnológica, A.C.,
78216 San Luis Potosí, SLP, México.
E-mail: jlrdz@ipicyt.edu.mx

Dr. D. B. U.
Laboratorio Avanzado de Nanoscopia Electrónica
Centro de Investigación y de Estudios Avanzados del I.P.N.
CINVESTAV, 07360 Mexico D.F., Mexico.

Dr. D. D.
Institut de Chimie Moléculaire et des Matériaux d'Orsay, UMR 8182 CNRS
Université Paris-Saclay, 91405 Orsay, France.

Dr. J. P. P. B.
Facultad de Ciencias Químicas, Universidad Autónoma de Chihuahua
Campus II, Chihuahua 31125, Chih., México.

Keywords: photocatalysis, hydrogen generation, solar fuels, bimetallic cocatalysts, synergetic effect

In this work, commercial titania (TiO_2-P25) is modified with mono- and bi-metallic (Au, Pd, and AuPd) nanoparticles synthesized by chemical reduction method using $NaBH_4$ as a strong reducing agent at room temperature. Bimetallic AuPd nanoalloys homogeneous in size and well dispersed on the TiO_2 surface are obtained. The charge carrier dynamics, which is a key factor in photocatalysis, is studied by Time Resolved Microwave Conductivity (TRMC). The results reveal that surface modification plays a crucial role in charge-carriers separation, increasing the activity under UV-visible light irradiation. The bimetallic AuPd nanoalloys formation is confirmed by High-Angle Annular Dark Field Scanning Transmission Electron Microscopy (HAADF-STEM) and corroborated by semiempirical molecular dynamics simulations (Gupta-LAMMPS). The surface-modified TiO_2 with bimetallic AuPd nanoalloys

exhibit higher photocatalytic activity compared to TiO_2 modified with their monometallic counterparts. Our experimental results are also supported by Density Functional Theory (DFT) and Density Functional Tight Binding (DFTB+) calculations, which show that alloying AuPd with low Pd content presents significant synergetic effects for hydrogen generation under UV-visible light from aqueous triethanolamine (TEOA) solutions. Additionally, the AuPd/TiO_2 photocatalysts are stable with cycling.

1. Introduction

Humanity is facing major crises such as air pollution and climate change. The exponential increase in global demand in energy, along with the growth of the world population, as well the still widely use of fossil fuels causes huge CO_2 emissions, responsible for greenhouse effects and climate change.[1] To mitigate these challenges, the development of renewable, clean energy sources is crucial for replacing fossil fuels and limiting CO_2 emissions, and hydrogen is projected to be not only the cleanest energy, it will also be consolidated as energy vector that moves us forward in the transition towards a zero carbon footprint, as committed by Hydrogen Europe, among other worldwide initiatives.

Since the petroleum crisis in 1973, alternatives have been sought for energy carriers like hydrogen.[2] Hydrogen as fuel produces higher energy power (122 kJg^{-1}) than gasoline (40 kJg^{-1}),[3] and can be obtained from different sources.[4] Currently, 95 % of hydrogen production comes from fossil fuels and only 5% from water electrolysis.[5] Recently, hydrogen production by solar water splitting has attracted much interest because it uses light energy and only emits water and oxygen.[6,7] Solar energy is a green, abundant and renewable source due to its natural availability, which offers a promising way to solve environmental and energy issues.[8,9] Hydrogen generation by photocatalytic water splitting requires a semiconductor with a bandgap energy wider than 1.23 eV (redox potential of water).[10,11] Titania (TiO_2) is a semiconductor widely used in photocatalysis because of its excellent properties such as high reactivity, photochemical and biological stability, low toxicity, and low price.[12,13] The limitation of TiO_2 application in photocatalysis is mainly due to the fast charge-carriers' recombination and its large band

gap (3.1-3.2 eV for anatase and rutile phases, respectively), which induces excitation only under UV light irradiation. However, UV light constitutes only 4 % of the solar light impinging on the Earth's surface.[14]

In this work, we used commercial titania (TiO_2-P25) as photocatalytic material because it is considered more stable and more efficient than other semiconductors at the adequate redox potentials for water splitting. TiO_2-P25 consists of a mixture of anatase-rutile crystalline phases and exhibits better photocatalytic activity than other types of TiO_2 due to the anatase-rutile heterojunction,[15,16] which is responsible of longer charge carriers' lifetime (compared to pure anatase phase) under UV excitation.[17,18,19] However, modification of titania for its activation under visible light is essential to better harvest solar light. Doping TiO_2 with plasmonic metal-NPs allows light absorption in the visible region of the spectrum due to the Localized Surface Plasmon Resonance (LSPR) phenomenon.[14,20,21] In addition, the photocatalytic activity under UV light is enhanced because the metal-nanoparticles (NPs) can act as electron traps inhibiting the charge carriers recombination.[14,22] The LSPR is the collective oscillation of conduction-free electrons excited by the incident photons in constructive interference with the electric field of the incident light.[23,24,25,26] The LSPR depends strongly on the metal nature, size, and morphology of the nanoparticles.[27,28,29] Among the noble metals, platinum (Pt) is the best co-catalyst for photocatalytic hydrogen generation.[29,30] However, Pt is costly and scarce, and thus, it is important to replace it with other more abundant metals, such as for example, gold (Au), that has been widely applied for photocatalytic hydrogen generation because it is an efficient cocatalyst, and it is also cheaper and more abundant than Pt. Au NPs can also activate TiO_2 under visible light due to its LSPR.[14]

Bimetallic nanoparticles like AuPd,[33,34] AuPt,[35,36], AuNi[26] and AuCu,[37,38] have been reported to demonstrate improvements in their electrical, optical, and catalytic properties. These nanoalloys exhibit superior catalytic performance, particularly in selectivity and stability, compared to their individual metal components. Therefore, they are highly desirable for a range of applications in catalysis and electrocatalysis.

Pd has gained attention due to its efficiency as catalyst in various applications, including catalytic and electrocatalytic processes, hydrogen storage, sensors, nanomedicine, hydrogenation reactions, C-C coupling reactions, mitigating environmental pollution and automotive emissions regulation.[34,42,43,44,45,46,47,48,49,50,51] Pd-Au bimetallic nanoparticles exhibit higher selectivity compared to monometallic Pd nanoparticles for hydrogenation reactions [34,40,41] Porous Pd_{shell}–Au_{core} nanostructures are very promising for application in direct ethanol fuel cells as they exhibit a very good electrocatalytic activity and a high stability.[44] Surface-modification of TiO_2 with bimetallic nanoparticles (NPs) based on gold has attracted much interest since higher activities for photocatalytic hydrogen generation can be obtained compared with their monometallic counterparts.[26,31,32,33]

Hereby, we report the application of AuPd nanoalloys on TiO_2 surface for hydrogen generation by photocatalysis, showing a synergetic effect under UV-visible light for H_2 production. The metal loading of both metals was optimized and the role of Au and Pd on the photocatalytic activity was studied using molecular simulations.

2. Results and Discussion

2.1 Alloying, Chemical Order and Electronic Structure Characterization

The morphology, size, elemental composition, and crystalline structure of 1 wt% AuPd/TiO_2 samples with the mass ratios of Au:Pd (9:1. 1:1. 1:9) were analyzed by TEM, HRTEM, and EDX techniques. TEM images in bright field (**Figures 1a**, **S1a**, and **S2a**) and *Z* contrast mode (**Figures 1b**, **S1b**, and **S2b**) show small and spherical AuPd-NPs with an average size of ~2.5-3 nm (**Figures 1e**, **S1e,** and **S2e**) well-dispersed on TiO_2 surface. **Table S1**, shows the AuPd-NPs average size for 1 wt% AuPd/TiO_2 samples with different mass ratios. HRTEM images of 1 wt% AuPd/TiO_2 samples show the localization of AuPd-NPs on the anatase phase (**Figure 1c**, **S1c,** and **S2c**). The electronic interaction with AuPd-NPs and the anatase phase inhibits the growth and agglomeration of the metal nanoparticles.[14] The interplanar distances were d=0.35 nm, corresponding to (101) planes of the anatase phase (JCPDS No. 21-1272). The

interplanar distances were measured using the Digital Micrograph software deduced by fast Fourier transformation process. The elemental composition was confirmed by EDX analysis showing the presence of Au, Pd, Ti, and Cu from the TEM grid (**Figure 1d**, **S1d,** and **S2d**). Small signals of Au and Pd were observed for 1 wt% Au_9Pd_1/TiO_2 and 1 wt% Au_1Pd_9/TiO_2 due to their low content, as shown in **Figure 1d** and **S2d**, respectively. Moreover, for the sample 1 wt% Au_1Pd_1/TiO_2, the EDX signals are almost identical due to the same metal content (**Figure S1d**).

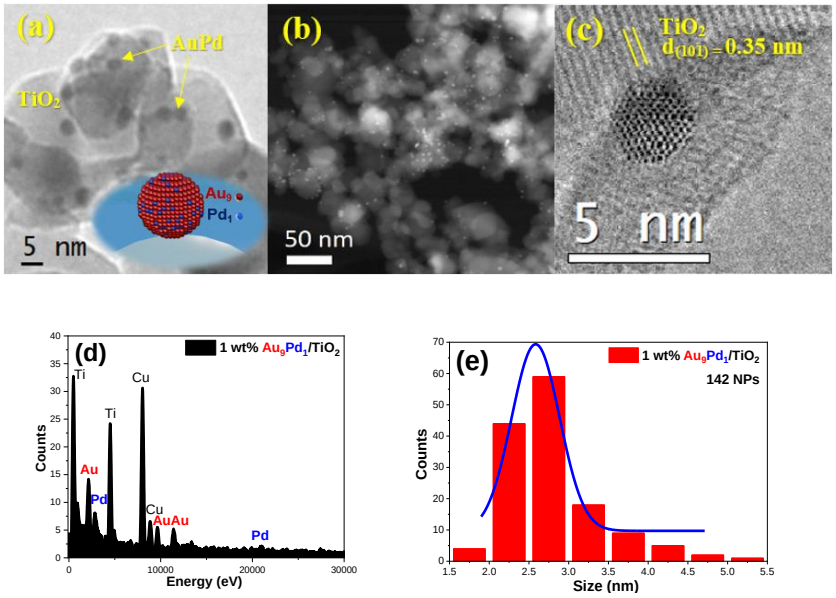

Figure 1. TEM micrographs of 1 wt% Au_9Pd_1/TiO_2 sample in **a)** bright field and **b)** Z contrast show spherical AuPd-NPs well-dispersed on TiO_2 surface, **c)** HRTEM micrograph showing the localization of AuPd-NPs on the anatase phase, **d)** EDS analysis showing the presence of the elements Au, Pd Ti, and Cu (from the TEM grid), **e)** histogram of AuPd-NPs showing an average size of ~2.6 nm.

In **Figure 2**, we present HAADF-STEM micrograph (**Figure 2a**) that shows Au_9Pd_1 nanoalloys with brighter tiny points corresponding to Au and less bright tiny spots corresponding to Pd (due to the highest atomic number of Au compared with Pd). Additionally, EDX analysis on single nanoparticles for the 1 wt% Au_9Pd_1/TiO_2 sample (**Figure 2b**) attests the presence of Pd on the surface of the nanoparticle, but with homogeneous distribution over all the structure (**Figure 2c**). In order to elucidate the chemical ordering of these alloys content, we performed a hybrid MD-MC (Molecular Dynamics-Monte Carlo, with the reliable Gupta interatomic potential for Au-Pd, see details in Supporting Information) simulation for each of the ratios, and then we simulated the line scan, shown in **Figure 2d** for the alloy content Au_9Pd_1: The simulation is in good agreement with the experimental results. Also, the results show that the alloy in all the systems is random, not ordered as in the AuPd bulk alloy previous studies.[60,61]

Inductively coupled plasma-optical emission spectrometry (ICP-OES) was utilized for elemental analysis, providing insights into the mass content of AuPd nanoalloys on TiO_2 surface, see **Table S2**.

The bimetallic photocatalysts 1 wt% $AuPd/TiO_2$ and bare TiO_2 were characterized by X-ray diffraction (XRD) to study the crystallinity of the samples (**Figure S3**). The diffracted peaks of the samples coincide with the reference peaks of the anatase and rutile crystalline phases, according to the data JCPDS files No. 21-1272 and No. 21-1276, respectively. The junction between anatase and rutile phases in P25 induces longer lifetime of the charge carriers increasing the photocatalytic activity.[62] No diffraction peaks were observed for AuPd-NPs due to the low metal loading and the small size of the NPs.[63]

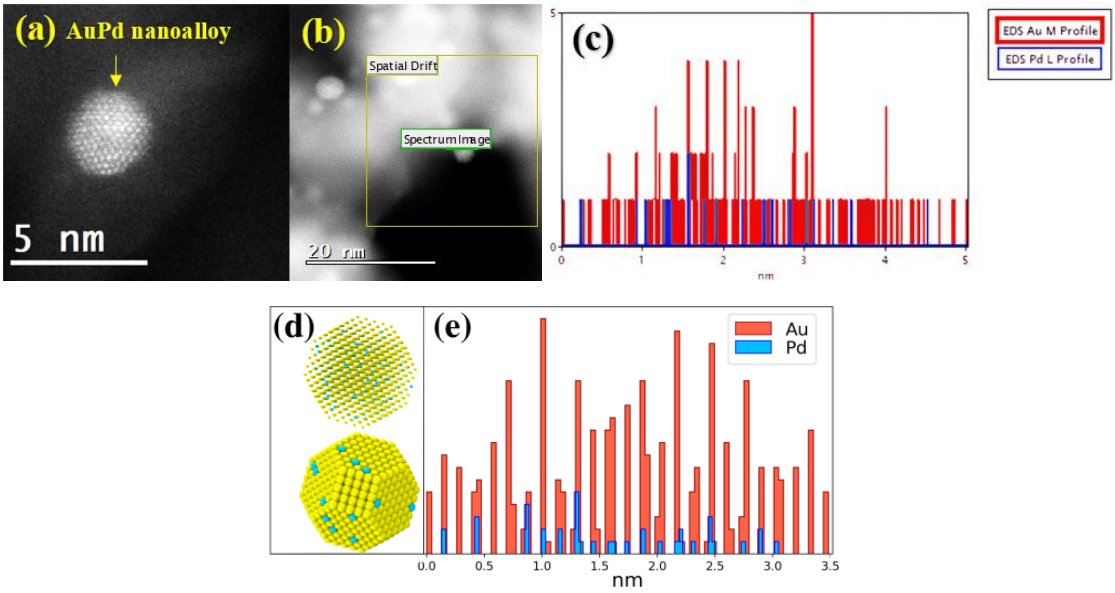

Figure 2. For the Au_9Pd_1 alloy, **a)** HAADF-STEM micrograph, **b)** Spectrum image and **c)** Au-M and Pd-L energy levels profiles. **d)** Energy optimization structure of Au_9Pd_1 NPs by hybrid MD-MC (Gupta) calculation for the identified size and structural shape from the experiment (a 1289 atoms cuboctahedron with ~3.5 nm); and **e)** simulated line scan on this nanoparticle and orientation shown, reflecting the chemical ordering.

The UV-vis spectra of the samples showed absorption in the UV region due to TiO_2 support (**Figures 3a-3c**). The UV-vis spectra of the monometallic samples Pd/TiO_2 show that the surface modification with Pd-NPs does not influence the TiO_2 bandgap (**Figure 3a**). Pd-NPs do not introduce energy levels in the bandgap, below the CB and above the VB because of their plasmon in the UV region.[57] Moreover, the monometallic samples of Au/TiO_2 show the surface plasmon resonance (LSPR) of gold with a maximum absorption peak at 553 nm, 547 nm, and 553 nm for 0.1 wt%, 0.5 wt% and 0.9 wt% Au/TiO_2 (**Figure 3b**). The dielectric constant of the TiO_2 support induces a shift of the LSPR of the metal nanoparticles toward larger wavelengths (compared to the NPs in water).[14,64] In the case of the bimetallic sample 1 wt% Au_9Pd_1/TiO_2 (**Figure 3c**), the LSPR of Au induces an intense and continuous absorption over the entire visible region due to the presence of AuPd nanoalloys rich in gold.[27] However, the sample 1 wt% Au_1Pd_9/TiO_2 does not show this characteristic because of the lowest content in gold. Au NPs act as visible absorption centers extending the light absorption of wide bandgap semiconductors to the visible

light due to their LSPR. Improving the UV-Vis absorption of the photocatalyst is important in photocatalysis to better harvest the solar light.

The band gap energies of the bimetallic samples and bare TiO_2 were calculated by the Tauc plot method, considering the indirect transition of anatase-phase.[16] **Figure 3d** shows the Tauc plots for bare TiO_2, 1 wt% Au_1Pd_9/TiO_2, 1 wt% Au_1Pd_1/TiO_2 and 1 wt% Au_9Pd_1/TiO_2. The estimated band gaps were 3.34 eV, 3.33 eV, 3.30 eV, and 3.30 eV, respectively. The optical band energy (E_g) can be determined by the following **Equations 1** and **2** for reflectance function *F(R)*, where *R* is the reflectance obtained by DRS, while *K* and *S* are the absorptions and scattering coefficients, respectively. *F(R)* is proportional to the absorption coefficient, where h is Planck's constant, ν is the photon's frequency, E_g is the band gap energy, and β is a factor depending on the transition probability and a constant in the optical frequency range. The *n* factor depends on the nature of the electron transition and is equal to 2 or 1/2 for the direct and indirect transition band gaps, respectively.

$$\mathrm{F(R)} = \frac{(1-\mathrm{R})^2}{2\mathrm{R}} = \frac{\mathrm{K}}{\mathrm{S}} \qquad (\mathbf{1})$$

$$(\mathrm{F(R)}h\nu)^{\mathrm{n}} = \beta\left(h\nu - E_g\right) \qquad (\mathbf{2})$$

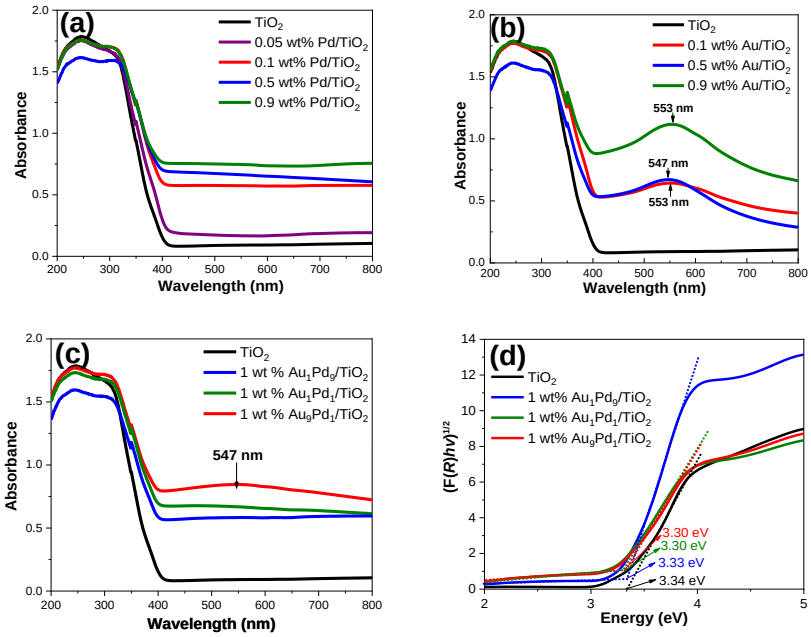

Figure 3. UV-vis DRS spectra of monometallic samples **a)** Pd/TiO_2 and **b)** Au/TiO_2, and bimetallic samples **c)** 1 wt% $AuPd/TiO_2$ and **d)** their corresponding Tauc plot.

TRMC signals of mono- and bimetallic photocatalysts and bare TiO_2 at 360 nm are shown in **Figure 4**. TRMC signals show I_{max} values reached for all the samples under UV light excitation, suggesting electron migration from the VB to the CB of TiO_2. Then, the I_{max} values decreased, and faster decays were observed for the mono- and bi-metallic photocatalysts than bare TiO_2. This can be explained by quick trapping by Au, Pd and AuPd nanoparticles of photogenerated electrons in the CB of TiO_2. **Figure 4a** shows the signals of Au/TiO_2 samples: The decay of the signal increases with the metal loading 0.9 wt% Au/TiO_2 > 0.5 wt% Au/TiO_2 > 0.1 wt% Au/TiO_2. In the case of Pd/TiO_2 samples (**Figure 4b**), the decay is not correlated with the metal loading and faster decay is obtained with 0.1 wt%. For the bimetallic photocatalysts (**Figure 4c**), the decay increases with 1 wt% Au_1Pd_1/TiO_2 > 1 wt% Au_9Pd_1/TiO_2 > 1 wt% Au_1Pd_9/TiO_2. These TRMC results indicate that the AuPd nanoalloys are efficient in electron scavenging reducing the charge-carrier recombination, which is beneficial for the photocatalytic activity. [14,37,58] At 420 nm (**Figure S4**), no signal from mono- and bimetallic samples was higher than the signal obtained by TiO_2. At 550 nm (**Figure S5**), the gold-based photocatalysts (mono- and bimetallic samples) show no

signal, indicating that at these wavelengths no hot electrons were detected in the CB of titania after Au-LSPR excitation.

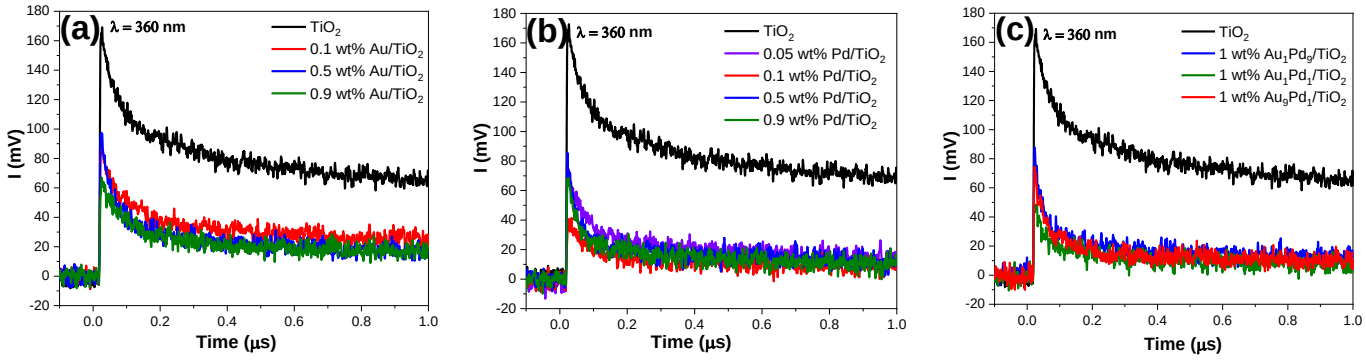

Figure 4. TRMC signals of monometallic photocatalysts **a)** Au/TiO_2, **b)** Pd/TiO_2 and **c)** bimetallic photocatalysts 1 wt% $AuPd/TiO_2$ at 360 nm with a laser energy of 1.2 mJ.

XPS analysis was performed on the sample surface in order to get information concerning the chemical environment of Au and Pd. The obtained Au-*4f* and Pd-*3d* core-level spectra are presented in **Figure 5**. Both Au-*4f* and Pd-*3d* doublets were fitted using asymmetrical line shapes derived from metallic Au and Pd references. The binding energy scale was calibrated based on Ti-$2p_{3/2}$ peak, used as internal reference, considered at 458.7 eV, which places the main O*1s* component corresponding to O in TiO_2 at 530 eV.[65] As a consequence, the spin-orbit coupling doublet of Au-*4f* is placed at 83.2 eV (Au-$4f_{7/2}$) and 86.8 eV (Au-$4f_{5/2}$) and that of Pd-*3d* at 334.5 eV (Pd-$3d_{5/2}$) and 339.8 eV (Pd-$3d_{3/2}$). This XPS analysis confirms that AuPd-NPs are in metallic states. In both cases, the binding energies of Au-*4f* and Pd-*3d* are shifted toward lower values from those given in the literature.[66] For instance, Au-$4f_{7/2}$ reported at 84 eV shifted to 83.2 eV and Pd-$3d_{5/2}$ from 335 eV to 334.5 eV. Two points can explain the shift towards lower binding energy values for Au-*4f* and Pd-*3d*, i.e., this first may be due to the interaction of the support (TiO_2) changing its electronic environment, the electron transfer from the TiO_2 to the AuPd-NPs,[37,63] and second, may be due to a strong electronic modification, and charge transfer between Au and Pd due to its nanoalloy formation.[67,68,69] Bimetallic AuPd nanoalloys have been reported to exhibit negative shifts in both the Au *4f* and Pd *3d* core levels.[70,71]

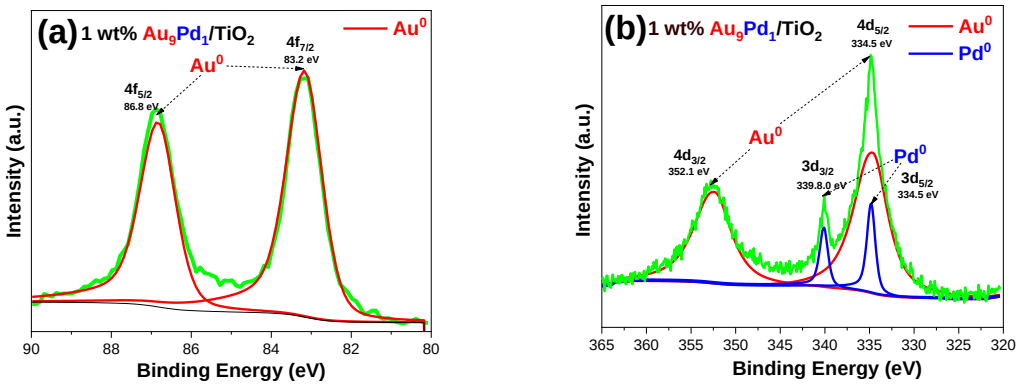

Figure 5. XPS spectra signals of 1 wt% Au_9Pd_1/TiO_2 sample, **a)** Au-*4f* core level, and **b)** Au-*4d* and Pd-*3d* core levels.

2.2. Photocatalytic Hydrogen Generation

The photocatalytic hydrogen generation for mono- and bi-metallic samples under UV-visible and visible light are shown in (**Figures 6a** and **6b)**, respectively. The monometallic samples present higher hydrogen generation rates than bare TiO_2 under UV-visible light (**Figure 6a**). The hydrogen generation rate for bare TiO_2 was 77.5 $\mu molg^{-1}h^{-1}$. The hydrogen generation rates for monometallic samples 0.1, 0.5 and 0.9 wt% Au/TiO_2 were 482.6, 534.4 and 788.6 $\mu molg^{-1}h^{-1}$, respectively. For 0.05, 0.1, 0.5 and 0.9 wt% Pd/TiO_2 metallic samples were 182.9, 1468.2, 1142.0, and 946.4 $\mu molg^{-1}h^{-1}$, respectively. The higher hydrogen generation rates of monometallic samples than bare TiO_2 is attributed to the work function: metals with higher work functions such as Pd (5.3 eV) and Au (5.1 eV) than the electron affinity of TiO_2 (4.0 eV) increase the Schottky barrier effect.[72] The Schottky barrier is formed due to the interface contact between Au and Pd-NPs (metallic system) and TiO_2 (semiconductor system).[73] The Schottky contact creates an internal electric field helping the electron-hole transfer and inhibiting the recombination process, which is confirmed by TRMC results (**Figure 4a** and **4b**).

Most importantly, **Figure 6a** shows higher hydrogen generation rates for bimetallic samples AuPd/TiO_2 compared with their monometallic counterparts. The hydrogen generation rates for 1 wt% Au_1Pd_9/TiO_2, 1 wt% Au_1Pd_1/TiO_2 and 1 wt% Au_9Pd_1/TiO_2 were 1534.6, 1822.2 and 2325.0 $\mu molg^{-1}h^{-1}$, respectively. The hydrogen generation increases with the Au/Pd ratio (1 wt% Au_9Pd_1/TiO_2 > 1 wt% Au_1Pd_1/TiO_2 > 1 wt%

Au_1Pd_9/TiO_2). The sample 1 wt% Au_9Pd_1/TiO_2 shows the highest activity with 2325.0 $\mu molg^{-1}h^{-1}$, which is ~30 times higher than bare TiO_2 (77.5 $\mu molg^{-1}h^{-1}$). The photocatalytic activity enhancement of the samples can be explained through their morphology, optical properties, crystallinity, and charge carrier dynamics. TEM images showed smaller AuPd-NPs on TiO_2 surface for 1 wt% Au_9Pd_1/TiO_2 sample (**Figure 1e**) than 1 wt% Au_1Pd_1/TiO_2 and 1 wt% Au_1Pd_9/TiO_2 samples. Smaller NPs have higher work function than larger NPs improving the Schottky barrier effect and therefore reducing the charge carriers' recombination.[14,72,73] TRMC results confirm that the AuPd nanoalloys are efficient in electron scavenging reducing charge-carrier recombinations and raising the photocatalytic activity under UV light excitation (**Figure 4c**). The decay increases when the TiO_2 surface is modified with AuPd nanoalloys. The reactive surface sites are well dispersed on the titania surface scavenging electrons in the CB of TiO_2 (which reduce H^+) inhibitting the charge carrier recombination, reducing and promoting the recombination of hydrogen atoms, and therefore raising the photocatalytic activity.

The photocatalytic hydrogen generation for mono- and bi-metallic samples under visible light is shown in **Figure 6b**. As previously stated, TiO_2 is not active under visible light. Pd/TiO_2 samples show negligible values for hydrogen generation under visible light. Pd-NPs do not modify the spectra of TiO_2 in the visible region due to their LSPR in the UV region (**Figure 3a**).[48,74] Moreover, Au/TiO_2 samples show photocatalytic activity under visible light due to their LSPR (**Figure 3b**). The hydrogen rates for 0.1, 0.5 and 0.9 wt% Au/TiO_2 samples were 2.4, 2.5, and 5.7 $\mu molg^{-1}h^{-1}$, respectively. Previous studies have shown that hot electrons can be injected from Au-NPs into the CB of TiO_2 under visible irradiation.[14] However, in our case, at 420 nm (**Figure S4a**) no signal was higher than the signal obtained with bare TiO_2. At 550 nm (**Figure S5a**), no detectable TRMC signals were obtained for Au/TiO_2 photocatalysts. This can be explained because the electron transfer is quite fast, and even if TRMC technique allows to obtain a signal at nanosecond scale, we cannot define the 10 first nanoseconds during the pulse.

The bimetallic samples $AuPd/TiO_2$ show higher hydrogen generation rates than the monometallic counterparts under visible light. The hydrogen generation rates for 1 wt% Au_1Pd_9/TiO_2, 1 wt%

Au_1Pd_1/TiO_2 and 1 wt% Au_9Pd_1/TiO_2 were 3.9, 8.5 and 13.0 $\mu molg^{-1}h^{-1}$, respectively. The optical properties were improved with higher Au/Pd ratio (1 wt% Au_9Pd_1/TiO_2) showing an intense and continuous absorption over the entire visible region (**Figure 3c**). Nevertheless, the same case occurs for bimetallic samples, no signal was higher than the signal obtained with TiO_2 at 420 nm (**Figure S4c**). At 550 nm (**Figure S5c**), no detectable TRMC signals were found. The photocatalytic activity under visible light suggests that hot electrons from Au NPs (in Au/TiO_2 and $AuPd/TiO_2$ samples) were injected into the CB of TiO_2 due to the activation of Au-LSPR after visible excitation.

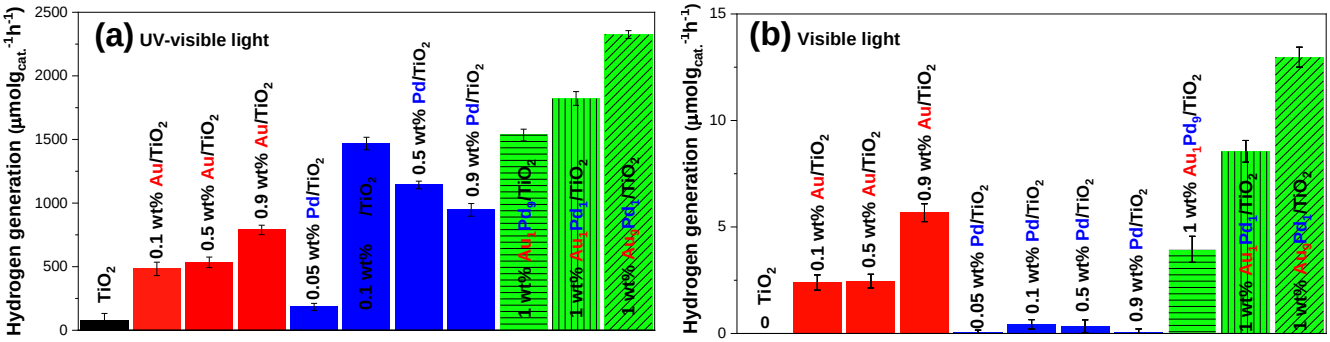

Figure 6. (a-b) Photocatalytic hydrogen generation for mono- and bimetallic photocatalysts and bare TiO_2 from 25 vol% TEOA aqueous solution under **a)** UV-visible and **b)** visible light.

Finally, decreasing the metal loading is important for large-scale hydrogen production due to the high cost of Au and Pd. The photocatalysts 0.1, 0.2, and 0.5 wt% $AuPd/TiO_2$ with mass ratios of Au:Pd (1:9, 1:1, 9:1) were tested under UV-visible light (**Figure 7**). The samples demonstrate similar activity as 1 wt% $AuPd/TiO_2$ samples.

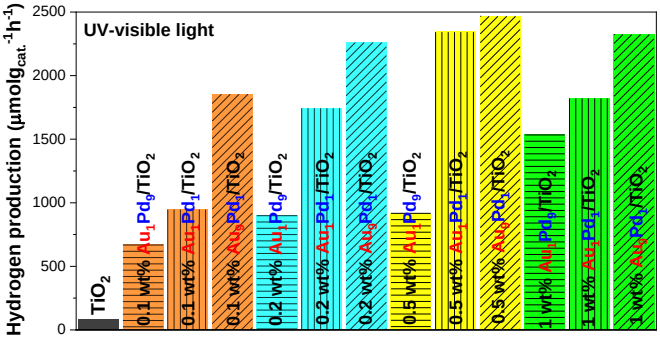

Figure 7. Photocatalytic hydrogen generation of bimetallic photocatalysts with metal loadings of 0.1, 0.2, 0.5 and 1 wt% AuPd/TiO_2 with mass ratios of Au:Pd (1:9, 1:1, 9:1) and bare TiO_2 from 25 vol% TEOA aqueous solution under UV-visible light irradiation.

The hydrogen generation increases with the ratio Au/Pd (Au_9Pd_1/TiO_2 > Au_1Pd_1/TiO_2 > Au_1Pd_9/TiO_2) for all the metal loadings. **Figure 8** presents a comparison between our optimal sample 0.5 wt% Au_9Pd_1/TiO_2 and 1 wt% Pt/TiO_2 (our sample benchmark with high photocatlytic activity, the Pt NPs are about 1 nm size and are well dispersed on TiO_2 surface), revealing quite similar (or slightly lower) photocatalytic activities. As we mentioned earlier, Pt is the best co-catalyst for photocatalytic hydrogen generation. Nevertheless, because of its high cost and limited abundance, replacing it with other more abundant metals is important. **Table S3**, compares the photocatalytic hydrogen generation under UV-visible light irradiation with data from literature. The comparison reveals notable differences in the efficiency of different catalysts under distinct conditions. However, compared to other reported studies, our work shows good photocatalytic activity under UV-visible radiation and a slight activity under visible light. Luna *et al*. obtained synergistic effects with bimetallic Au-Ni and Ni-Pd NPs for hydrogen generation.[26,29] Also, Su *et al.* reported strong synergistic effects with 1 wt% $Pd_{shell}Au_{core}/TiO_2$ for photocatalytic hydrogen generation with a specific wavelength at 365 nm (UV LED) using a variety of important feedstock chemicals. Nevertheless, they did not show any activity under visible light.[33]

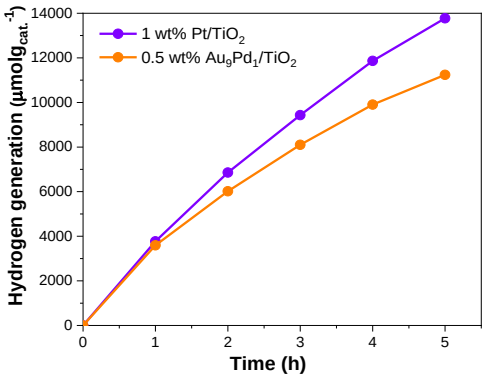

Figure 8. Comparison of the photocatalytic hydrogen generation of 0.5 wt% Au_9Pd_1/TiO_2 with 1 wt% Pt/TiO_2 from 25 vol% TEOA aqueous solution under UV-visible light irradiation.

2.3 Density Functional Theory (DFT) calculations

To improve the understanding of the higher hydrogenation rates in the case of bimetallic systems, the adsorption of two hydrogen atoms on a model of Au-NP and Au_9Pd_1-NP was investigated at the DFT and DFTB+ quantum levels (see Methods and Supporting Information for computational details). First, for DFT calculations, the optimized geometries show a different adsorption mode on the metal surface, with each H atom remaining on one Au for Au-NP, and with one H atom on gold and the other H shared between the Pd and the neighbouring gold atoms ("Au-H-Pd") for Au_9Pd_1-NP. This structural change corresponds to different bond lengths, resulting in different electronic effects (**Table S5**). The Au-Pd and Au-Au bond lengths around the shared H in the bimetallic cluster are shorter than Au-Au distances in Au-NP. In addition, the Au-H and Pd-H distances are longer in Au_9Pd_1-NP for the shared H atom, leading to a weaker hydrogen adsorption strength. The analysis of the electron density shows Au-H and Pd-H bonds with a valence electronic population basin of 1.7 electron and 1.6 electron for Au-H and Au-H-Pd, respectively. The strength of the bond was evaluated to be close to a single covalent bond with a Mayer bond order of 0.86 for Au-H in Au-NP, and much weaker with a Mayer bond order of 0.37 for Au-H-Pd in Au_9Pd_1-NP. This lower hydrogen atom adsorption strength for the bimetallic system may be one explanation for the higher reactivity.

2.3 Density Functional Tight Binding (DFTB+) calculations

By DFTB+ using the GFN1-xTB parameterization, we performed molecular dynamics simulations of H atoms with many different arrays (as described in Supplementary Information) over the surface of optimized clusters (N=38 atoms, with cuboctahedral shape) for the three Au_9Pd_1, Au_1Pd_1, and Au_1Pd_9

alloys. The systems were brought to a temperature of 298 K and then left at constant temperature during 20 picoseconds, and the main results are hereby briefly presented.

The case of Au_9Pd_1 was the only system that led to the formation of H_2, while for none (among 11 systems built) of the systems in the Au_1Pd_9 case did the formation of H_2 occur. According with previous DFT results, it seems that when the amount of Pd is higher, the hydrogen atomes are strongly attracted to Pd, and thus their movement is restricted. For the case of Au_1Pd_1, the formation of H_2 also occurs for one system (among 9 built), however, we notice that the inclusion of H in these 1:1 systems seems to destabilize them (even more than the obtained structures after the energy optimization process), since most of the calculated systems end up suffering a considerable deformation of the nanoparticle. More details are given in the Supplementary Information file.

2.4 Proposed Photocatalytic Mechanism

Charge carriers' dynamics, which is a key factor in photocatalysis was studied by TRMC.[14,29,31,57,58,59] At 360 nm excitation, the mono- and bimetallic systems and bare TiO_2 are activated meaning that electrons migrate to the CB of TiO_2, reaching I_{max} values. Moreover, when the surface of TiO_2 is modified with mono- and bi-metallic nanoparticles, the I_{max} value decreases compared with bare TiO_2 (**Figure 4**). This indicates that the metal nanoparticles act as electron traps, inhibiting the charge carriers' recombination. The electron migration from CB of TiO_2 to the metal nanoparticles occurs due to the work function and Schottky junction, which creates an internal electric field helping the electron-hole transfer and inhibiting the recombination process.[75,76] **Figure 9a** shows a scheme of the photocatalytic mechanism under UV light excitation for bimetallic AuPd/TiO_2 sample.

$$TiO_2 \xrightarrow{h\nu > E_g} TiO_2(e^-_{CB} + h^+_{VB}) \qquad (\mathbf{3})$$

$$H_2O + e^- \rightarrow H_2 + OH^- \qquad (\mathbf{4})$$

$$H^+ + e^- \rightarrow H^{\cdot} \qquad (\mathbf{5})$$

$$H^{\cdot} + H^{\cdot} \rightarrow H_2 \qquad (\mathbf{6})$$

At 420 nm excitation, hot electrons are injected from AuPd nanoalloys to the CB of TiO_2 due to the Au-LSPR excitation.[14] Water molecules or H^+ are reduced on the TiO_2 surface by the electrons to produce H_2 (**Figure 9b**), as we mentioned before. Finally, to inhibit the oxidation reaction generated by the photogenerated holes in the VB of TiO_2 and AuPd-NPs an electron donor was used (TEOA in our study), which scavenges the holes to generate H_2 (**Equations 7-10**).[77] TEOA can self-sustain the photocatalytic hydrogen generation process, which can be obtained from industrial organic effluents related to dry cleaning, cosmetics, shampoos, detergents, surfactants, textiles, and water repellents.[77]

$$TiO_2(h^+) + OH^- \rightarrow OH^{\bullet} \qquad (\mathbf{7})$$

$$TiO_2(h^+) + H_2O \rightarrow OH^{\bullet} + H^+ \qquad (\mathbf{8})$$

$$TEOA + OH^{\bullet} \rightarrow HCHO + NH_3 \qquad (\mathbf{9})$$

$$HCHO + OH^{\bullet} \rightarrow H_2 \qquad (\mathbf{10})$$

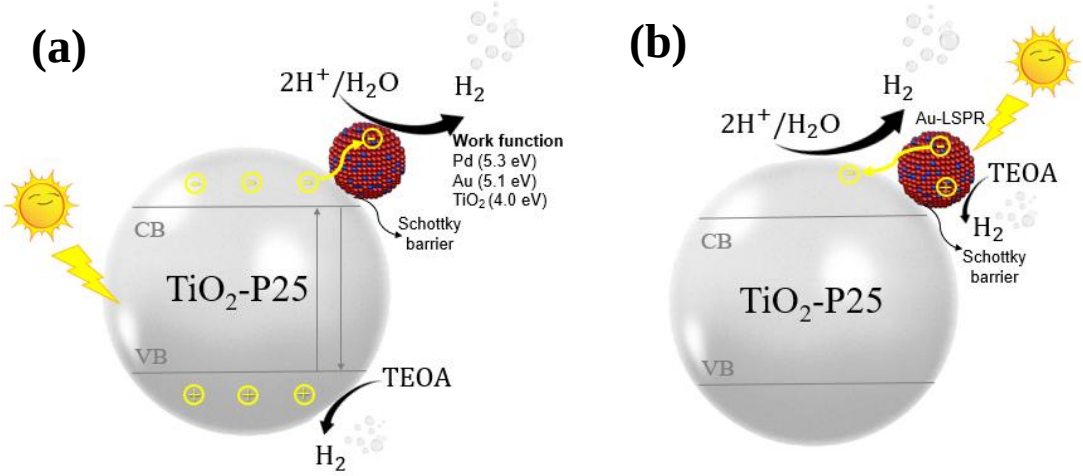

Figure 9. Proposed photocatalytic mechanism of bimetallic AuPd/TiO_2 samples under **a)** UV, and **b)** visible light irradiation.

2.5 Stability with cycling

Finally, the photocatalyst stability was investigated for the 0.5 wt% Au_9Pd_1/TiO_2 sample, which demonstrated a stable photocatalytic activity with a slight decrease with cycling (**Figure 10**). The dispersion of AuPd nanoalloys, morphology, size, and crystalline structure were analysed before and after cycling (**Figure S6**). TEM images in dark field show the AuPd-NPs well-dispersed on the TiO_2 surface before and after cycling (**Figures S6a** and **S6d**). HAADF-STEM micrographs show that the AuPd nanoalloys are quite stable after cycling, showing brighter tiny points corresponding to Au due to its highest atomic number and less brightness tiny spots corresponding to Pd (**Figures S6b** and **S6e**). The interplanar distance of 0.23 nm corresponds to (111) plane of Au (**Figure S6c**) and the one of 0.2 nm corresponds to the plane (200) of Au (**Figure S6f**). The interplanar distances of 0.18 nm (**Figures S6c** and **S6f**) and 0.16 nm (**Figure S6c**) can be assigned to (200) and (211) planes of the anatase phase (JCPDS No. 21-1272), respectively. However, the AuPd-NPs size increases from ~2.5-2.7 nm to ~3.0-3.2 nm after cycling (**Figure S6g**). This metal nanoparticles' sintering probably explains the slight decrease in photocatalytic hydrogen generation due to larger-NPs decreasing the work function and diminishing the Schottky barrier effect, increasing charge carriers' recombination. The surface chemical composition and oxidation states of AuPd nanoalloys on the TiO_2 surface were analyzed by XPS after cycling. The comparison of the XPS spectra for 0.5 wt% AuPd/TiO_2 sample before and after cycling for Au-*4f* and Pd-*3d* states are shown in **Figures S6h** and **S6i**, respectively. After cycling, the XPS spectra are noisy compared to those before cycling. This can be attributed to metal loss after recovering the powder by centrifugation.

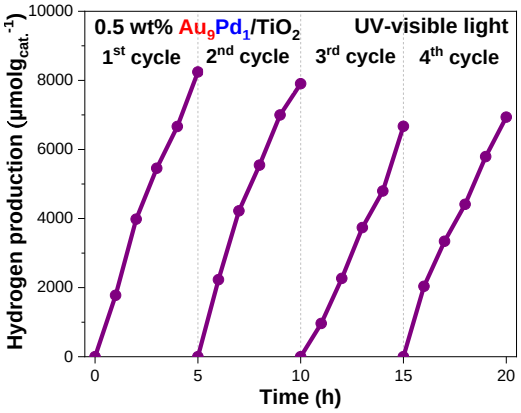

Figure 10. The photocatalyst stability of 0.5 wt% Au_9Pd_1/TiO_2 sample from 25 vol% TEOA aqueous solution under UV-visible light irradiation.

3. Conclusion

In summary, AuPd nanoalloys homogeneous in size (~2.5-3 nm) were deposited on the TiO_2 surface by chemical reduction method using $NaBH_4$ at room temperature. The AuPd nanoalloys formation was confirmed by HAADF-STEM and hybrid MD-MC calculations validated this alloy structure. Synergetic effects were obtained with the AuPd nanoalloys: the bimetallic AuPd/TiO_2 samples show higher photocatalytic activity for H_2 generation under UV-visible light irradiation compared with their monometallic counterparts. The photocatalytic hydrogen generation enhancement of bimetallic samples was explained through their morphology, optical properties, crystallinity, charge carrier dynamics, electronic structure (DFT) and molecular dynamics (DFTB+) calculations. The Au_9Pd_1/TiO_2 sample is the most active and it is quite stable with cycling, with a slight decrease in hydrogen generation. TRMC results demonstrated that the surface modification of TiO_2 with bimetallic AuPd nanoalloys (electron traps) plays a role in charge-carrier separations increasing the activity under UV light irradiation. AuPd nanoalloys can be used as efficient cocatalysts for hydrogen generation with an activity comparable with that of Pt co-catalysts.

4. Experimental Section

4.1 Chemical reagents

Commercial titanium dioxide (TiO_2-P25, 80% anatase, and 20% rutile, Evonik) was used as photocatalytic support. Gold (III) chloride trihydrate ($HAuCl_4 \cdot 3H_2O$, Sigma Aldrich, 99.9%), palladium (II) chloride ($PdCl_2$, Sigma Aldrich, 99%) and platinum (II) acetylacetonate ($Pt(C_5H_7O_2)_2$, Sigma Aldrich, 97%) were used as metal precursors. Sodium borohydride ($NaBH_4$, Sigma Aldrich ≥ 99%), and triethanolamine ($C_6H_{15}NO_3$, Sigma-Aldrich ≥ 99%) were used as reducing agent and hole scavenger, respectively. Deionized water (Milli-Q 18.2 MΩ) was used in all experiments.

4.2 Photocatalysts Synthesis

The photocatalysts were synthesized by chemical reduction using $NaBH_4$ as reducing agent at room temperature (**Figure S7**). Mother solutions of 0.01 M $HAuCl_4$ (30 mL) and 0.01 M $PdCl_2$ (30 mL) were prepared. In a flask, 10 mL of deionized water were added to 250 mg of TiO_2 under vigorous stirring for 30 min. Afterwards, an amount of each salt precursor solution was added to the dispersed TiO_2 aqueous suspension to prepare photocatalysts with different metal loadings keeping the vigorous stirring for 1 h. Immediately a fresh aqueous solution of 2 mL $NaBH_4$ 1 M was prepared in an ice-water bath because $NaBH_4$ reacts violently and quickly with water at room temperature. Freezing water slows the reaction sufficiently enough to allow the reduction of metal ions. Subsequently, 0.5 mL of $NaBH_4$ 1 M was added to the mixture, maintaining vigorous stirring for 2 h. After, the photocatalysts were washed with deionized water and separated by centrifugation three times at 6500 rpm for 10 min to remove the non-reduced, undesired ions, then dried at 60°C for 48 h. The supernatants were transparent, indicating that most of the metals were deposited on the titania support. The UV-vis spectra of the supernatants were flat (**Figure S8**) compared with the solutions of the

salt precursors of $HAuCl_4$ and $PdCl_2$. The Au^{III} and Pd^{II} complexes were reduced by $NaBH_4$ in aqueous solutions at room temperature. The redox potentials are E_{Au^{3+}/Au^0}=1.5 V *vs.* NHE, E_{Pd^{2+}/Pd^0}=0.83 V *vs*. NHE,[52] and E^0=−1.24 V *vs.* NHE.[53,54] The concentration of $NaBH_4$ is a crucial factor in the synthesis, higher concentration induces the reduction of the nanoparticle size.[55]

Mono- and bi-metallic (Au/TiO_2, Pd/TiO_2 and $AuPd/TiO_2$) samples were prepared with 1 wt% metal loading for comparison (**Table S4**). The monometallic photocatalysts containing Au and Pd were respectively purple and gray, and the color is more intense with the metal loading (**Figure S9**). The bimetallic photocatalysts 1 wt% Au_1Pd_9/TiO_2 and 1 wt% Au_1Pd_1/TiO_2 were gray in color. For 1 wt% Au_9Pd_1/TiO_2, the color was gray-purple. Later, the bimetallic photocatalysts with total metal loading of 0.1 wt%, 0.2 wt%, and 0.5 wt% $AuPd/TiO_2$ were synthesized using the same mass ratios to study the effect of the loading on the photocatalytic activity. Finally, Pt/TiO_2 was synthesized (the best co-catalyst for hydrogen generation) to compare with the bimetallic samples $AuPd/TiO_2$. The 1 wt% Pt/TiO_2 sample was prepared by the radiolysis method. This method is very powerful to synthesize metal NPs of controlled size and shape in solution and on support.[56,57] Platinum (II) acetylacetonate was used as salt precursor and ethanol as solvent. The solution was stirred one hour, sonicated for five minutes, degassed with Ar gas (Air Liquide) and then irrradiated using a ^{60}Co panoramic gamma source. The dose used was 3.2 kGy, which is sufficient for complete reduction of Pt^{II} complexes (at a concentration of 10^{-3} M) to their zerovalent state Pt^0. After the radiolysis process, the photocatalyst was separated by centrifugation and dried at 60°C for 24 h to remove any remaining traces of the solvent.

4.3 Photocatalysts Characterization

The optical properties were analyzed by Diffuse Reflectance Spectroscopy (DRS) with a UV-Vis-NIR spectrophotometer (Cary 5000 Series, Agilent Technologies) recorded from 200 nm to 800 nm region. The crystal structure of the synthesized photocatalysts was investigated by X-ray diffraction (XRD) using a SmartLab RIGAKU with Cu K_α radiation, 40 kV, 44 mA, λ = 0.15406 nm over the 2Θ range from 20° to 80°, with steps of 0.01° s^{-1}. Transmission Electron Microscopy (TEM) FEI TECNAI F30 microscope equipped with a tungsten field emission gun operated at 300 keV was used to study the morphology, size, and dispersion of bimetallic AuPd-NPs over the TiO_2 surface, equipped with an Energy-dispersive X-ray spectroscopy (EDS) detector to identify the elemental composition of the samples. The AuPd nanoalloy formation and crystalline structure was analyzed by High-Angle Annular Dark Field Scanning Transmission Electron Microscopy (HAADF-STEM) using a High-Resolution Transmission Electron Microscopy (HR-TEM), model JEOL 200F (200 keV). The powder samples were dissolved in 2-propanol under sonication, and then few drops of the solution were deposited on a holey carbon-coated copper grid (300 mesh). The surface elemental composition and oxidation states were studied by X-ray Photoelectron Spectroscopy (XPS). XPS measurements were performed on a *K*-Alpha spectrometer from ThermoFisher, equipped with a monochromated X-ray Source (Al K_α, 1486.68 eV) with a spot size of 400 µm, corresponding to an irradiated area of ~ 1 mm^2. The samples were measured in the powder form. The base pressure was $3x10^{-9}$ mbar. The hemispherical analyzer was operated in CAE (Constant Analyzer Energy) mode, with pass energy of 200 eV and a step of 1 eV for the acquisition of surveys spectra, and pass energy of 50 eV and a step of 0.1 eV for the acquisition of narrow spectra. A “dual beam” flood gun was used to neutralize the charge

build-up. The binding energies were calibrated against the neutral carbon binding energy set at 284.8 eV. The precision in binding energy is ± 0.2 eV. The spectra were recorded and treated by means of Avantage software provided by Thermo Fisher. The fitting procedure implied the use of assymetrical lineshapes after the extraction of a Shirley-type background.

The photogenerated charge-carrier dynamics, which is a key factor in photocatalysis was studied by Time Resolved Microwave Conductivity (TRMC) technique for the bimetallic samples under UV and visible light excitations. A pulsed and tunable laser source (200 to 2000 nm) equipped with an optical parametric oscillator (OPO; EKSPLA, NT342B) was used to excite the samples, and a Gunn diode (30 GHz) was used to generate microwaves. The principle of this technique has been described in previous papers.[14,29,31,57,58,59] TRMC technique measures the relative change ($\frac{\Delta P(t)}{p}$) in microwave power reflected from a semiconductor material during its excitation by a laser pulse. This change ($\Delta\sigma(t)$) could be related to small perturbation of the sample's conductivity (**Equation 11**).

$$\frac{\Delta P(t)}{p} = A\Delta\sigma(t) = Ae\mu_e\Delta n_e(t) \qquad \textbf{(11)}$$

In TiO_2-based compounds, the electron mobility （μ_e） is much higher than the holes. Therefore, $\Delta\sigma(t)$ is mainly due to excess electrons in the CB. $\Delta n_e(t)$ is the excess free electrons number at time *t*. *A* (sensitivity factor) is time-independent and relies on the conductivity of the semiconductor and the microwave frequency. The main data provided by the TRMC technique gives the maximum value of the signal (I_{max}), which corresponds to the number of excess free electrons generated by the laser pulse. The signal decay $I(t)$ (denominated photoconductivity) as a function of time (in μs or *ns*) is owing to the decrease of excess electrons after the laser pulse by charge carriers' recombination or trapping.[14,29,31,57,58,59]

4.4 Photocatalytic hydrogen generation tests

The photocatalytic hydrogen generation tests were performed in a closed quartz reactor. 20 mg of the photocatalyst were dispersed in 20 mL of 25-vol% of triethanolamine (TEOA) aqueous solution. TEOA was used as a sacrificial electron donor (or hole scavenger). Before irradiation, the reactor was degassed with Ar for 20 min under vigorous stirring. After, the samples were irradiated for 5 h using a Peschl photoreactor and a Xenon Lamp 300 W LOT-Oriel (250 to 2000 nm) equipped with a water filter (a large quartz cell) between the lamp and the reactor to screen the infrared light and avoid heating of the samples. An optical filter was used to limit the irradiation to the visible ($\lambda \geq 420$ nm). The hydrogen amount was measured by gas chromatography every hour (Micro GC Fusion, INFICON). The photocatalyst stability is an essential parameter that defines the materials' commercial significance. For the photocatalyst stability, 20 mg of photocatalyst were once again dispersed in 20 mL of 25-vol% of TEOA aqueous solution. The mixture was degassed with Ar for 20 minutes under vigorous stirring before exposure to irradiation for 5 h in a Peschl photoreactor. The powder was recovered through centrifugation and dried at 60°C for 24 h. After, the photocatalyst was weighted and dispersed in a 25-vol% TEOA aqueous solution, maintaining a 1 mg mL^{-1} ratio. This process was repeated for 4 cycles.

5. Methods

The geometry optimization calculations were carried out at the DFT level using the ORCA 5.0.3 software.[78] The PBE GGA functional was used in association with dispersion corrections in the D3 framework proposed by Grimme with the addition of the Becke–

Johnson damping (D3BJ).[79] The SDD pseudopotential (with 19 and 18 valence-electrons treated explicitly for Au and Pd atoms, respectively) and the associated basis set were used for the metal atoms, and the def2-SVP basis set was used for hydrogen atoms. The quantum chemical analyses were performed with the Multiwfn code by analyzing the electron density generated from ORCA.[80] The electron localization function (ELF) was calculated to determine the valence basins.[81]

An hybrid molecular dynamics and Monte Carlo approach (MD-MC) was used for obtain the chemical order of the three NPs alloys concentrations, based on interatomic Gupta potential and using LAMMPS code.[82,83] For the reactivity dynamics of H_2 on alloys NPs, DFTB+ with the GFN1-xTB parameterization was used[84,85], previosly optimizing the structures with the hybrid MD-MC methodology. See the Supporting Information for details.

Supporting Information

Supporting Information is available from the Wiley Online Library or from the author.

Acknowledgements

Ana Andrea Méndez-Medrano acknowledges the financial support from CONACYT-Mexico (grant 995288) and to CAMPUS FRANCE scholarship from the French Embassy in Mexico A.A. Méndez-Medrano acknowledges also the National Laboratory Research in Nanoscience and Nanotechnology (LINAN), IPICYT, Dr. Héctor Gabriel Silva Pereyra for TEM-EDS characterization. M.C. Beatriz Adriana Rivera-Escoto, and Dr. Ignacio Guadalupe Becerril Juárez for XRD characterization. Also, we acknowledge Mireille Benoit for her help at the Institut de Chimie Physique laboratory. DFT calculations were performed using computational resources from the “Mésocentre” computing center of Université Paris-Saclay, CentraleSupélec and École Normale Supérieure Paris-Saclay supported by CNRS and Région Île-de-France.

Conflict of Interest
The authors declare no conflict of interest.
Author Contributions
Data Availability Statement
The data that support the findings of this study are available from the corresponding authors upon reasonable request.

Received: ((will be filled in by the editorial staff))
Revised: ((will be filled in by the editorial staff))
Published online: ((will be filled in by the editorial staff))

References

[1] H. Ahmad, S. K. Kamarudin, L. J. Minggu, M. Kassim, *Renew. Sust. Energ. Rev.*, **2015**, 43, 599.

[2] S. Protti, A. Albini, N. Serpone, *Phys. Chem. Chem. Phys.*, **2014**, 16, 19790.

[3] Y. Piña-Pérez, J. E. Samaniego-Benitez, F. Tzompantzi, L. Laurtundo-Rojas, A. Garcia-Garcia, A. Mantilla, G. Romero-Ortiz, *Mater. Lett.*, **2022**, 330, 133205.

[4] I. K. Kapdan, F. Kargi, *Enzyme. Microb. Technol.*, **2006**, 38, 569.

[5] S. E. Hosseini, M. A. Wahid, *Renew. Sust. Energ. Rev.*, **2016**, 57, 850.

[6] T. N. Veziroğlu, S. Şahin, *Energy Convers. Manag.*, **2008**, 49, 1820.

[7] S. Sharma, S.K. Ghoshal, *Renew. Sust. Energ. Rev.*, **2015**, 43, 1151.

[8] B. A. Pinaud, J. D. Benck, L. C. Seitz, A. J. Forman, Z. Chen, T. G. Deutsch, B. D. James, K. N. Baum, G. N. Baum, S. Ardo, H. Wang, E. Miller, T. F. Jaramillo, *Energy Environ. Sci.*, **2013**, 6, 1983.

[9] X. Chen, S. S. Mao, *Chem. Rev.*, **2007**, 107, 2891.

[10] A. Kudo, Y. Miseki, *Chem. Soc. Rev.*, **2009**, 38, 253.

[11] H. Hennig, *Angew. Chem. Int. Ed.*, **2015**, 54, 4429.

[12] X. Yuan, D. Floresyona, P. H. Aubert, T. T. Bui, S. Remita, S. Ghosh, F. Brisset, F. Goubard, H. Remita, *Appl. Catal. B.*, **2019**, 242, 284.

[13] J. Ma, J. Dai, Y. Duan, J. Zhang, L. Qiang, J. Xue, *Renew. Energy*, **2020**, 156, 1008.

[14] M. G. Méndez-Medrano, E. Kowalska, A. Lehoux, A. Herissan, B. Ohtani, S. Rau, C. Colbeau-Justin, J. L. Rodríguez-López, H. Remita, *J. Phys. Chem. C*, **2016**, 120, 25010.

[15] B. Ohtani, O. O. Prieto-Mahaney, D. Li, R. Abe, *J. Photochem. Photobiol.*, **2010**, 216, 179.

[16] J. Zhang, P. Zhou, J. Liu, J. Yu, *Phys. Chem. Chem. Phys.*, **2014**, 16, 20382.

[17] R. Ma, T. Chen, *J. Phys. Chem. C*, **2019**, 123, 19479.

[18] V. Etacheri, M. K. Seery, S. J. Hinder, S. C. Pillai, *Adv. Funct. Mater.*, **2011**, 21, 3744.

[19] A. Di Paola, G. Cufalo, M. Addamo, M. Bellardita, R. Campostrini, M. Ischia, R. Ceccato, L. Palmisano, *Colloids Surf.*, **2008**, 317, 366.

[20] E. Grabowska, A. Zaleska, S. Sorgues, M. Kunst, A. Etcheberry, C. Colbeau-Justin, H. Remita, *J. Phys. Chem. C*, **2013**, 117, 1955.

[21] M. G. Méndez-Medrano, E. Kowalska, A. Lehoux, A. Herissan, B. Ohtani, D. Bahena, V. Briois, C. Colbeau-Justin, J. L. Rodríguez-López, H. Remita, *J. Phys. Chem. C.*, **2016**, 120, 5143.

[22] M. G. Méndez-Medrano, E. Kowalska, B. Ohtani, D. Bahena Uribe, C. Colbeau-Justin, S. Rau, J. L. Rodríguez-López, H. Remita, *J. Chem. Phys.*, **2020**, 153, 034705.

[23] V. Kumaravel, S. Mathew, J. Bartlett, S.C. Pillai, *Appl. Catal. B.*, **2019**, 244, 1021.

[24] N. S. Ibrahim, W. L. Leaw, D. Mohamad, S. H. Alias, H. Nur, *Int. J. Hydrog. Energy*, **2020**, 45, 28553.

[25] M. Ismael, *Sol. Energy*, **2020**, 211, 522.

[26] A. L. Luna, E. Novoseltceva, E. Louarn, P. Beaunier, E. Kowalska, B. Ohtani, M. A. Valenzuela, H. Remita, C. Colbeau-Justin, *Appl. Catal. B.*, **2016**, 191, 18.

[27] P. Verma, Y. Kuwahara, K. Mori, H. Yamashita, *J. Mater. Chem. A.*, **2016**, 4, 10142.

[28] A. Zielińska-Jurek, *J. Nanomater.*,**2014**, 2014, 208920.

[29] A. L. Luna, D. Dragoe, K. Wang, P. Beaunier, E. K. Kowalska, B. Ohtani, D. B. Uribe, M. A. Valenzuela, H. Remita, C. Colbeau-Justin, *J. Phys. Chem. C*, **2017**, 121, 14302.

[30] M. Luo, P. Lu, W. Yao, C. Huang, Q. Xu, Q. Wu, Y. Kuwahara, H. Yamashita, *ACS Appl. Mater. Interfaces*, **2016**, 8, 20667.

[31] A. L. Luna, F. Matter, M. Schreck, J. Wohlwend, E. Tervoort, C. Colbeau-Justin, M. Niederberger, *Appl. Catal. B.*, **2020**, 267, 118660.

[32] X. Gan, D. Lei, *Coord. Chem. Rev.*, **2022**, 469, 214665.

[33] R. Su, R. Tiruvalam, A. J. Logsdail, Q. He, C. A. Downing, M. T. Jensen, N. Dimitratos, L. Kesavan, P. P. Wells, R. Bechstein, H. H. Jensen, S. Wendt, C. R. A. Catlow, C. J. Kiely, G. J. Hutchings, F. Besenbacher, *ACS Nano*, **2014**, 8, 3490.

[34] T. Redjala, H. Remita, G. Apostolescu, M. Mostafavi, C. Thomazeau, D. Uzio, *Oil Gas Sci. Technol.*, **2006**, 61, 789.

[35] F. Wang, Y. Jiang, D. J. Lawes, G. E. Ball, C. Zhou, Z. Liu, R. Amal, *ACS Catal.*, **2015**, 5, 3924.

[36] M. Mirdamadi-Esfahani, M. Mostafavi, B. Keita, L. Nadjo, P. Kooyman, H. Remita, *Gold Bull.*, **2010**, 43, 49.

[37] Z. Hai, N. El Kolli, D. B. Uribe, P. Beaunier, M. José-Yacaman, J. Vigneron, A. Etcheberry, S. Sorgues, C. Colbeau-Justin, J. Chen, H. Remita, *J. Mater. Chem. A.*, **2013**, 1, 10829.

[38] Z. Hai, N. El Kolli, J. Chen, H. Remita, *New J. Chem.*, **2014**, 38, 5279.

[39] F. Ksar, L. Ramos, B. Keita, L. Nadjo, P. Beaunier, H. Remita, *Chem. Mater.*, **2009**, 21, 3677.

[40] F. R. Lucci, M. T. Darby, M. F. G Mattera, C. J. Ivimey, A. J. Therrien, A. Michaelides, M. Stamatakis, E. C. H. Sykes, *J. Phys. Chem. Lett.*, **2016**, 7, 480.

[41] N. Dimitratos, G. Vilé, S. Albonetti, F. Cavani, J. Fiorio, N. López, L. M. Rossi, R. Wojcieszak, *Nat. Rev. Chem.*, **2024, 8**, 195.

[42] F. Ksar, G. K. Sharma, F. Audonnet, P. Beaunier, H. Remita, *Nanotechnol.*, **2011**, 22, 305609.

[43] F. Ksar, G. Surendran, L. Ramos, B. Keita, L. Nadjo, E. Prouzet, P. Beaunier, A. Hagège, F. Audonnet, H. Remita, *Chem. Mater.*, **2009**, 21, 1612.

[44] G. Surendran, F. Ksar, L. Ramos, B. Keita, L. Nadjo, E. Prouzet, P. Beaunier, P. Dieudonné, F. Audonnet, H. Remita, *J. Phys. Chem. C*, **2008**, 112, 10740.

[45] S. Ghosh, S. Bera, N. Karmakar, R. N. Basu, *Mater. Today: Proc.*, **2018**, 5, 9733.

[46] S. Ghosh, A. L. Teillout, D. Floresyona, P. De Oliveira, A. Hagège, H. Remita, *Int. J. Hydrogen Energy*, **2015**, 40, 4951.

[47] A. Dumas, P. Couvreur, *Chem. Sci.*, **2015**, 6, 2153.

[48] I. Sarhid, I. Abdellah, C. Martini, V. Huc, D. Dragoe, P. Beaunier, I. Lampre, H. Remita, *New J. Chem.*, **2019**, 43, 4349.

[49] D. Astruc, *Inorg. Chem.*, **2007**, 46, 1884.

[50] B. Karimi, S. Abedi, J. H. Clark, V. Budarin, *Angew. Chem. Int. Ed.*, **2006,** 45, 4776.

[51] S. K. Min, N. Kim, M. P. Cheon, S. L. Jae, Y. K. Kyung, J. Park, *Org. Lett.*, **2005**, 7, 1077.

[52] M. Sahoo, S. Mansingh, S. Subudhi, P. Mohapatra, K. Parida, *Catal. Sci. Technol.*, **2019**, 9, 4678.

[53] S. Carregal-Romero, J. Pérez-Juste, P. Hervés, L. M. Liz-Marzán, P. Mulvaney, *Langmuir*, **2010**, 26, 1271.

[54] A. M. Pasqualeti, P. Y. Olu, M. Chatenet, F. H. B. Lima, *ACS Catal.*, **2015**, 5, 2778.

[55] Q. M. Liu, D. B. Zhou, Y. Yamamoto, R. Ichino, M. Okido, *Trans. Nonferrous Met. Soc. China*, **2012**, 22, 117.

[56] P. Ray, M. Clément, C. Martini, I. Abdellah, P. Beaunier, J. L. Rodriguez-Lopez, V. Huc, H. Remita, I. Lampre, *New. J. Chem.*, **2018**, 42, 14128.

[57] O. Tahiri Alaoui, A. Herissan, C. Le Quoc, M. E. M. Zekri, S. Sorgues, H. Remita, C. Colbeau-Justin, *J. Photochem. Photobiol.*, **2012**, 242, 34.

[58] H. Remita, M. G. Méndez-Medrano, C. Colbeau-Justin, *Visible Light-Active Photocatalysis*, Ghosh, S. (Ed.) Wiley-VCH **2018**, pp. 129-164.

[59] C. Wang, D. Dragoe, C. Colbeau-Justin, P. Haghi-Ashtiani, M. N. Ghazzal, H. Remita, *ACS Appl. Mater. Interfaces.*, **2023**, 15, 42637.

[60] F. Berthier, B. Legrand, *J. Condens. Matter Phys*., **2020**, 32, 354001.

[61] F. Berthier, J. Creuze, T. Gabard, B. Legrand, M. C. Marinica, C. Mottet, *Phys. Rev. B*, **2019**, 32, 014108.

[62] Y. Mi, Y. Weng, *Sci. Rep.*, **2015**, 5, 11482.

[63] J. B. Chang, C. H. Liu, J. Liu, Y. Y. Zhou, X. Gao, S. D. Wang, *Nanomicro Lett.*, **2015**, 7, 307.

[64] S. Nishimura, N. Abrams, B. A. Lewis, L. I. Halaoui, T. E. Mallouk, K. D. Benkstein, J. van de Lagemaat, A. J. Frank, *J. Am. Chem. Soc.*, **2003**, 125, 6306.

[65] M. C. Biesinger, B. P. Payne, A. P. Grosvenor, L. W. M. Lau, A. R. Gerson, R. S. C. Smart, *Appl. Surf. Sci.*, **2011**, 257, 2717.

[66] J. F. Moulder, W. F. Stickle, P. E. Sobol, K. D. Bomben, J. Chastain, *Handbook of X-ray Photoelectron Spectroscopy*, Perkin-Elmer, **1992**.

[67] F. Wang, H. Zhang, Z. Zhang, Q. Ma, C. Kong, S. Min, *J. Colloid Interface Sci.*, **2022**, 607, 312.

[68] B. Liu, K. Li, Y. Luo, L. Gao, G. Duan, *J. Chem. Eng.*, **2021**, 420, 129881.

[69] J. Xu, T. White, P. Li, C. He, J. Yu, W. Yuan, Y.F. Han, *J. Am. Chem. Soc.*, **2010**, 132, 10398.

[70] É. Casey, J. D. Holmes, G. Collins, *ACS Appl. Nano Mater.*, **2022**, 5, 16196.

[71] X. Zhu, Q. Guo, Y. Sun, S. Chen, J. Q. Wang, M. Wu, W. Fu, Y. Tang, X. Duan, D. Chen, Y. Wan, *Nat. Commun.*, **2019**, 10, 1428.

[72] Y. Zhang, O. Pluchery, L. Caillard, A. F. Lamic-Humblot, S. Casale, Y. J. Chabal, M. Salmeron, *Nano Lett.*, **2015**, 15, 51.

[73] L. Lechaptois, Y. Prado, O. Pluchery, *Nanoscale*, **2023**, 15, 7510.

[74] S. de Marchi, S. Núñez-Sánchez, G. Bodelón, J. Pérez-Juste, I. Pastoriza-Santos, *Nanoscale*, **2020**, 12, 23424.

[75] H. J. Le, D. van Dao, Y. T. Yu, *J. Mater. Chem. A.*, **2020**, 8, 12968.

[76] B. L. Sharma, *Metal-Semiconductor Schottky Barrier Junctions and Their Applications*, Plenum Press, New York, **1984**.

[77] P. Chowdhury, H. Gomaa, A. K. Ray, *Chemosphere*, **2015**, 121, 54.

[78] F. Neese, *Wiley Interdiscip. Rev. Comput. Mol. Sci.*, **2012**, 2, 73.

[79] S. Grimme, S. Ehrlich, L. Goerigk, *J. Comput. Chem.*, **2011**, 32,1456.

[80] T. Lu, F. Chen, *J. Comput. Chem.*, **2012**, 33, 580.

[81] A. D. Becke, K. E. A. Edgecombe, *J. Chem. Phys.*, **1990**, 92, 5397.

[82] F. Pittaway, L. O. Paz-Borbón, R. L. Johnston, H. Arslan, R. Ferrando, C. Mottet, G. Barcaro, A. Fortunelli, *J. Phys. Chem. C*, **2009**, 113, 21, 9141.

[83] A. P. Thompson, H. M. Aktulga, R. Berger, D. S. Bolintineanu, W. M. Brown, P. S. Crozier, P. J. in 't Veld, A. Kohlmeyer, S. G. Moore, T. D. Nguyen, R. Shan, M. J. Stevens, J. Tranchida, C. Trott, S. J. Plimpton, *Comput. Phys. Commun.*, **2022**, 271, 108171.

[84] B. Hourahine, B. Aradi, V. Blum, F. Bonafé, A. Buccheri, C. Camacho, C. Cevallos, M. Y. Deshaye, T. Dumitrică, A. Dominguez, S. Ehlert, M. Elstner, T. van der Heide, J. Hermann, S. Irle, J. J. Kranz, C. Köhler, T. Kowalczyk, T. Kubař, I. S. Lee, V. Lutsker, R. J. Maurer, S. K. Min, I. Mitchell, C. Negre, T. A. Niehaus, A. M. N. Niklasson, A. J. Page, A.

Pecchia, G. Penazzi, M. P. Persson, J. Řezáč, C. G. Sánchez, M. Sternberg, M. Stöhr, F. Stuckenberg, A. Tkatchenko, V. W.-z. Yu, T. Frauenheim, *J. Chem. Phys.*, ***2020***, 152, 124101.

[85] S. Grimme, C. Bannwarth, P. Shushkov, *J. Chem. Theory Comput.*, **2017**, 13, 5, 1989.

Table of Contents

Ana Andrea Méndez-Medrano, Daniel Bahena-Uribe, Diana Dragoe, Carine Clavaguéra, Christophe Colbeau-Justine, Juan Pedro Palomares Báez, José Luis Rodríguez-López, and Hynd Remita**

Enhanced Photocatalytic Activity of Surface-Modified TiO_2 with Bimetallic AuPd Nanoalloys for Hydrogen Generation

Surface-modified TiO_2 with bimetallic AuPd nanoalloys exhibit high photocatalytic activity for H_2 production. Alloying Au with low Pd content presents significant synergetic effects for hydrogen generation under UV—visible light. These findings are supported by molecular quantum level calculations.